Lee *et al. Int J Concr Struct Mater* (2021) 15:6
https://doi.org/10.1186/s40069-020-00440-x

International Journal of Concrete Structures and Materials

RESEARCH Open Access

Investigation of Diagonal Strut Actions in Masonry-Infilled Reinforced Concrete Frames

Seung-Jae Lee[1], Tae-Sung Eom[1*] and Eunjong Yu[2]

Abstract

This study analytically investigated the behavior of reinforced concrete frames with masonry infills. For the analysis, VecTor2, a nonlinear finite element analysis program that implements the Modified Compression Field Theory and Disturbed Stress Field Model, was used. To account for the slip behavior at the mortar joints in the masonry element, the hyperbolic Mohr–Coulomb yield criterion, defined as a function of cohesion and friction angle, was used. The analysis results showed that the lateral resistance and failure mode of the infilled frames were significantly affected by the thickness of the masonry infill, cohesion on the mortar joint–brick interface, and poor mortar filling (or gap) on the masonry boundary under the beam. Diagonal strut actions developed along two or three load paths on the mortar infill, including the backstay actions near the tension column and push-down actions near the compression columns. Such backstay and push-down actions increased the axial and shear forces of columns, and ultimately affect the strength, ductility, and failure mode of the infilled frames.

Keywords: masonry infill, infilled frame, equivalent strut, finite element analysis, seismic performance

1 Introduction

Reinforced concrete moment frames with unreinforced masonry infills (or infilled frames) have been used in many existing buildings such as school and government facilities in Korea (see Fig. 1). Such masonry infill walls are considered as nonstructural elements because they do not carry gravity loads; however, under earthquake loads, the masonry infill walls significantly affect the seismic performance of the infilled frames; during the initial behavior before cracking, the masonry infill with large shear rigidity significantly increases the lateral stiffness; after shear cracking, diagonal cracks and consequent compression struts that occur on the masonry infill change load paths and ultimately affect the strength and ductility.

The behavior of the infilled frames becomes more complicated due to deformation compatibility between the flexure-dominated frame members and shear-dominated masonry infill wall. Such interaction may be evaluated either by tests or by sophisticated analysis methods. From a practical view point, it is also possible to use simplified approaches, such as equivalent strut models (ATC 1998; ASCE/SEI 41-17). Many researchers have proposed various equivalent strut models to account for interaction (or force transfer) between the masonry infill and adjacent frame members, and investigated the validity of such strut models on the basis of tests and analyses (Stafford-Smith 1966; Paulay and Priestley 1992; Crisafulli 1997; Al-Chaar 2002; Dolsek and Fajfar 2002; El-Dakhakhni et al. 2003; Park et al. 2012; Yu et al. 2016). However, such strut models may not be accurate in representing the behavior and failure mode of infilled frames; furthermore, the estimation of the effective strut width often relies on empirical formula or case-specific experimental data. Considering that the behavior of infilled frames varies with design variables, such as material properties, aspect ratio, and the size and location of openings, finite element analysis is more suitable to account for the effects of such design variables than the strut models.

*Correspondence: tseom@dankook.ac.kr
[1] Dept. of Architectural Engineering, Dankook Univ., 152 Jukjeon-ro, Gyeonggi 16890, Korea
Full list of author information is available at the end of the article
Journal information: ISSN 1976-0485 / eISSN 2234-1315

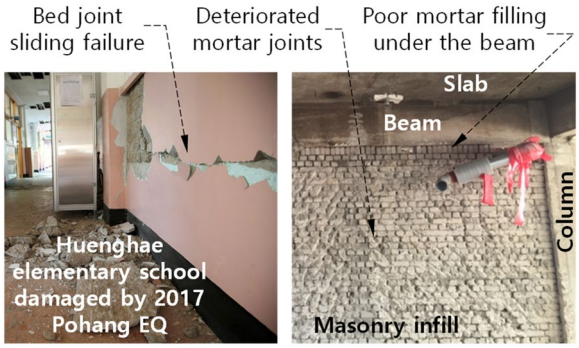

Fig. 1 Reinforced concrete frames with masonry infills.

Two approaches can be used for finite element analysis of masonry walls and masonry-infilled frames. The first approach is to separately model brick units, mortar joints, and interfaces, considering failure mechanisms (Lourenco and Rots 1997; Mehrabi and Shing 1997; Stavridis and Shing 2010; Zhai et al. 2017). Stavridis and Shing (2010) and Zhai et al. (2017) investigated finite element analysis methods for masonry structures, based on the plasticity theory and discrete constitutive models for materials and their interface. Diagonal, horizontal, and vertical interface elements were used to account for various failure modes occurring along the concrete cracks and mortar joints. The second approach is to consider the masonry element as a homogeneous continuum where material properties such as brick units and mortar joints are smeared over a finite region (Lourenco et al. 1998; Facconi et al. 2014, 2018). Facconi et al. (2014, 2018) developed the disturbed stress field model (DSFM) for masonry that accounts for the slip behavior occurring along the mortar joints. The DSFM and analytical procedure for concrete and masonry elements have been implemented in a nonlinear finite element program, VecTor2 (Wong et al. 2013).

This study investigated the behavior of infilled frames through nonlinear analysis by VecTor2. For this purpose, the DSFM for masonry (Facconi et al. 2014) that accounts for the orthotropic behavior of brick units and the slip behavior on the mortar joint–brick interface was reviewed. Then, by performing nonlinear analysis, the force transfer mechanism and failure mode of the infilled frames varying with the thickness of the masonry infill and poor mortar filling on the masonry boundary under the beam, were investigated. In particular, by comparing the distributions of cracks and diagonal struts on the masonry infill at various loading stages, the effects of such diagonal strut actions on the masonry infill-frame interaction and column shear failure were studied.

2 Finite Element Modeling for Masonry

2.1 Disturbed Stress Field Model for Masonry Element

Figure 2 shows the concept of the DSFM for unreinforced masonry element (Facconi et al. 2014; Wong et al. 2013). Basically, the DSFM is formulated based on average stresses and strains over a finite region. The stresses of a masonry element, denoted as σ_{m1} and σ_{m2} (or σ_{mx}, σ_{my}, and τ_{mxy}), are related to the net strains of the masonry continuum, ε_{m1} and ε_{m2} (or ε_{mx}, ε_{my}, and γ_{mxy}), which do not include slip deformation at the mortar joint. Figure 2b shows the

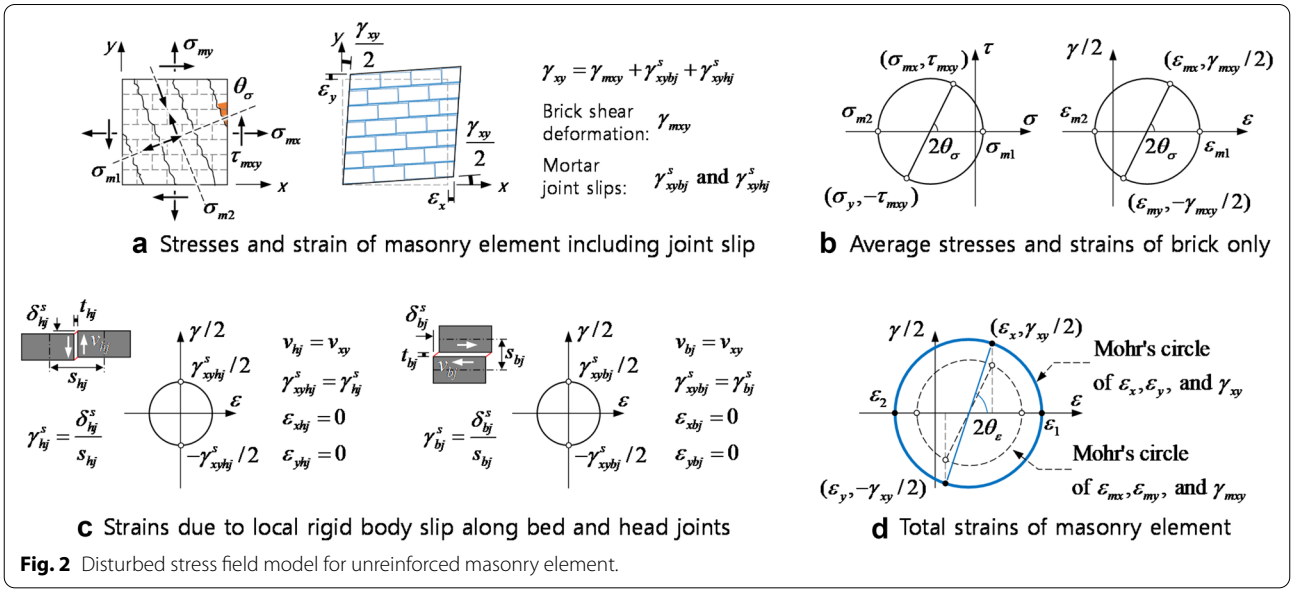

Fig. 2 Disturbed stress field model for unreinforced masonry element.

Mohr's stress and strain circles for the masonry element. The direction of principal stresses of the masonry element, θ_σ, is defined as follows (see Fig. 2b):

$$\theta_\sigma = \frac{1}{2}\tan^{-1}\left(\frac{\gamma_{mxy}}{\varepsilon_{mx}-\varepsilon_{my}}\right). \quad (1)$$

In Fig. 2b, the principal stresses σ_{m1} and σ_{m2} corresponding to the principal strains ε_{m1} and ε_{m2}, respectively, are determined from the uniaxial stress–strain relationship of the masonry material. Unlike the concrete panel where slip deformation occurs along the crack plane, slip in the masonry element occurs along the interface of the bed and head mortar joints as the shear stress reaches the yield state. Thus, the DSFM for the masonry element does not consider the shear stress and deformation occurring along the crack plane that is associated with the principal stresses. Instead, as shown in Fig. 2c, the shear stress τ_{mxy} and corresponding slip deformations $\delta_{bj}{}^s$ and $\delta_{hj}{}^s$ that occur along the head and bed joints of brick units, respectively, are taken into account. Consequently, the total strains of the masonry element, ε_x, ε_y, and γ_{xy}, are determined by adding the additional strains due to the bed and head joint slips $\delta_{bj}{}^s$ and $\delta_{hj}{}^s$ to the masonry continuum strains ε_{mx}, ε_{my}, and γ_{mxy}. Such additional slip strains are denoted as $\varepsilon_{xbj}{}^s$, $\varepsilon_{ybj}{}^s$, $\gamma_{xybj}{}^s$, $\varepsilon_{xhj}{}^s$, $\varepsilon_{yhj}{}^s$, and $\gamma_{xyhj}{}^s$ in Fig. 2a and c. The direction θ_ε of the principal strains ε_1 and ε_2, which is different from θ_σ in Eq. (1), is then determined using ε_x, ε_y, and γ_{xy}, as follows:

$$\theta_\varepsilon = \frac{1}{2}\tan^{-1}\left(\frac{\gamma_{xy}}{\varepsilon_x-\varepsilon_y}\right). \quad (2)$$

The orthotropic behavior of the masonry element after cracking is considered by the uniaxial compression and tension relationships, σ_{m2}–ε_{m2} and σ_{m1}–ε_{m1} relationships, respectively (Facconi et al. 2014). Such uniaxial behavior of the masonry element is similar to that of concrete. The compressive strength of the masonry element varies with the angle of the principal compressive stress (=f_{m2}) relative to the bed joint, θ_σ; according to the compression failure criteria originally formulated by Ganz (1986) and reformulated by Facconi et al. (2014), such masonry strength (i.e., the maximum value of σ_{m2} in Fig. 2b) can be defined as functions of σ_{m2}/σ_{m1}. In addition, the compressive strength of the cracked masonry element decreases with the tensile strain ε_{m1} transverse to the cracking (i.e., compression softening behavior, Lofti and Shing 1991). To account for variations of such masonry strength, the DSFM defines the effective compressive strength f_{me} as follows:

$$f_{me} = \beta_d \beta_m f'_m, \quad (3)$$

where β_d (≤ 1.0) is the reduction factor that accounts for compressive softening due to ε_{m1}; β_m (≤ 1.0) is the factor that accounts for the effects of the direction of the principal stress f_{m2} relative to the bed joint (i.e., θ_σ); and $f_m{}'$ is the compressive strength of the masonry element in the transverse direction to the bed joint. Note that β_m is defined as functions of the masonry compressive strengths f_{mx} and f_{my} in the transverse directions to the head and bed joints, respectively, masonry tensile strengths f_{tx} and f_{ty} in the transverse directions to the head and bed joints, respectively, and the cohesion and friction angle on the interface of the mortar joint (c and ϕ, respectively). β_d and β_m are presented in Facconi et al. (2014) and Wong et al. (2013) as follows:

$$\beta_d = \frac{1}{1+0.55C_d} \leq 1.0, \quad (4)$$

$$C_d = \begin{cases} 0 \text{ for } r < 0.28 \\ 0.35(r-0.28)^{0.8} \text{ for } r \geq 0.28 \end{cases}, \quad (5)$$

$$\beta_m = \frac{f_{m2}(f_{m1},\theta)}{f_{my}} \leq 1.0, \quad (6)$$

where $r=\varepsilon_{m2}/\varepsilon_{m1}$ and f_{m2} (f_{m1},θ) is the maximum masonry strength obtained from the Ganz's failure criteria.

The orthotropic behavior of the uncracked masonry element is considered, using the elastic moduli E_{mx} and E_{my} and the Poisson's ratio ν_{xy}. After cracking, the elastic modulus E_m that accounts for the orthotropic behavior of the cracked masonry element is defined to have transition from E_{my} at $\theta_\sigma=0°$ to E_{mx} at $\theta_\sigma=90°$ (Wong et al. 2013).

3 Slip Model for Mortar Joint

According to Atkinson et al. (1989) and Rots (1997), slip behavior on the mortar joint–brick interface is affected by the normal stress on the interface and the fracture energy that releases when slip occurs. In the DSFM for the masonry element, as shown in Fig. 3a, the shear behavior of the mortar joints is idealized as an elastic–perfectly plastic relationship, defined by the shear modulus G_m ($=0.5E_{my}/[1+\nu_{xy}]$) and maximum shear strength v_m. The maximum shear strength v_m on the mortar joint–brick interface is determined using the following hyperbolic Mohr–Coulomb yield criterion (see Fig. 3b):

$$F(\sigma_{nj}) = v_m^2 + \mu^2(\sigma_{nj}-f_{tj})^2 + 2\rho(\sigma_{nj}-f_{tj}) = 0, \quad (7)$$

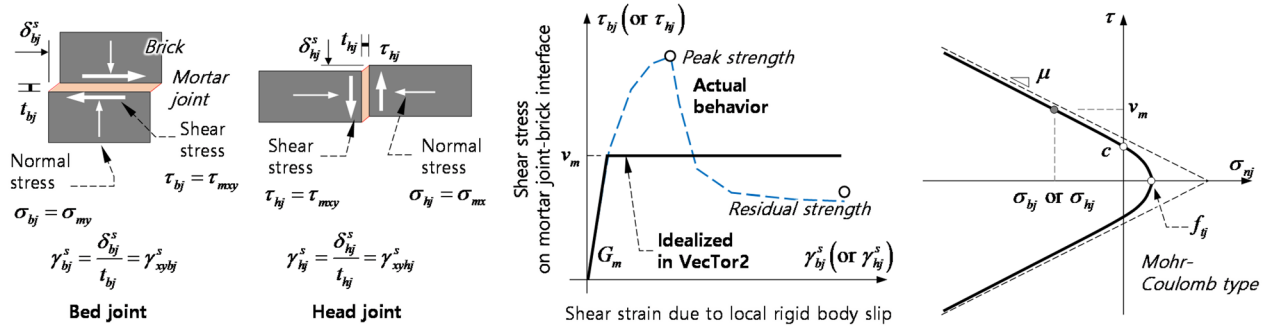

a Shear stress and slip deformation at the bed and head joints **b** Hyperbolic yield criterion

Fig. 3 Shear slip model for mortar joints.

where μ (=tan ϕ) and ϕ are the friction coefficient and angle on the mortar joint interface; σ_{nj} is the normal stress acting on the interface (i.e., σ_{mx} and σ_{my} for the head and bed joints, respectively, see Fig. 2a); f_{tj} = tensile strength of the mortar joint–brick interface; ρ is the radius of curvature of the yield curve at the vertex of the hyperbola, defined as $[c^2 - (\mu t_{tj})^2]/[2t_{tj}]$; and c is the cohesion on the mortar joint–brick interface. Note that even after slip occurs on the interface, the maximum shear strength v_m may increase or decrease, depending on σ_{nj}.

The slip behavior of the mortar joint–brick interface is affected by the cohesion c and friction coefficient μ (or friction angle ϕ) (see Fig. 3b). In general, the cohesion and friction coefficient have ranges of $c = 0.1$ MPa–1.5 MPa and $\mu = 0.3$–1.2 (or $\phi = 16.7°$–$50°$) (Paulay and Priestley 1992). Figure 3b compares the actual and idealized shear stress–slip responses on the mortar joint–brick interface under monotonic loading (Angelillo et al. 2014; Rahman and Ueda 2014). In VecTor2, the pre-peak slip response is considered as linear elastic with the shear modulus G_m, whereas the post-peak response is approximated as perfectly plastic with the maximum shear stress v_m. If the mortar joint–brick interface is subjected to cyclic loading and the shear stress on the interface is reversed repeatedly, damage such as cracking accumulates near the interface and consequently the cohesion and friction coefficient on the mortar joint–brick interface may decrease under cyclic loading. This indicates that, when assessing or designing infilled frames, care needs to be taken not to overestimate the shear stress–slip behavior on the interface. In Eurocode 6 (ECS 2005), the cohesion and friction coefficient are taken as $c = 0.1$ MPa ~ 0.4 MPa and $\mu = 0.75$ (or $\phi \approx 37°$), respectively; such design values are closer to the residual strength on the mortar joint–brick interface, than the peak strength.

4 Model Validation for Masonry-Infilled Frames

4.1 Details of Masonry-Infilled Frame Specimens

To investigate the validity of the DSFM and hyperbolic Mohr–Coulomb yield criterion for masonry elements, nonlinear analysis was performed for three reinforced concrete frames with or without masonry infill, BF, IF0.5, and IFS0.5 (Kim et al. 2016). IF0.5 and IFS0.5 are the infilled frames, whereas BF is the bare reinforced concrete frame. In the specimen names, '0.5′ indicates the thickness of masonry infill was 90 mm (i.e., half of the width of the brick unit, 0.5B), and 'S' indicates that there was a clearance of 35 mm on the masonry boundary under the beam (i.e., poor mortar filling). Thus, for IFS0.5, the boundaries on both sides of the masonry infill were in contact with the columns, whereas the boundary on the top was not in contact with the beam.

Figure 4 shows the configuration and section details of the infilled frame specimens. The story height measuring from the top of the base to the center of the beam was $h = 1750$ mm and the bay length between the columns (i.e., center-to-center distance) was $l = 2500$ mm. The aspect ratio was $l/h = 1.43$. The cross-sections of the column and beam were 300 mm × 300 mm and 300 mm × 350 mm in size, respectively. For the column, eight D16 bars (diameter 15.9 mm) were used for longitudinal reinforcement and square hoops of D10 bars (diameter 9.5 mm) were used at a spacing of 150 mm for transverse reinforcement. For the beam, four D16 bars were used at the top and bottom as flexural reinforcement, and rectangular hoops of D10 bars were used at a spacing of 150 mm as shear reinforcement. The columns and beams were lightly reinforced members, not satisfying the requirements of intermediate and special moment frame members specified in KBC 2016 (AIK 2016). For IF0.5 and IFS0.5, the masonry infills (thickness 90 mm) were placed inside the frame. The size of solid cement

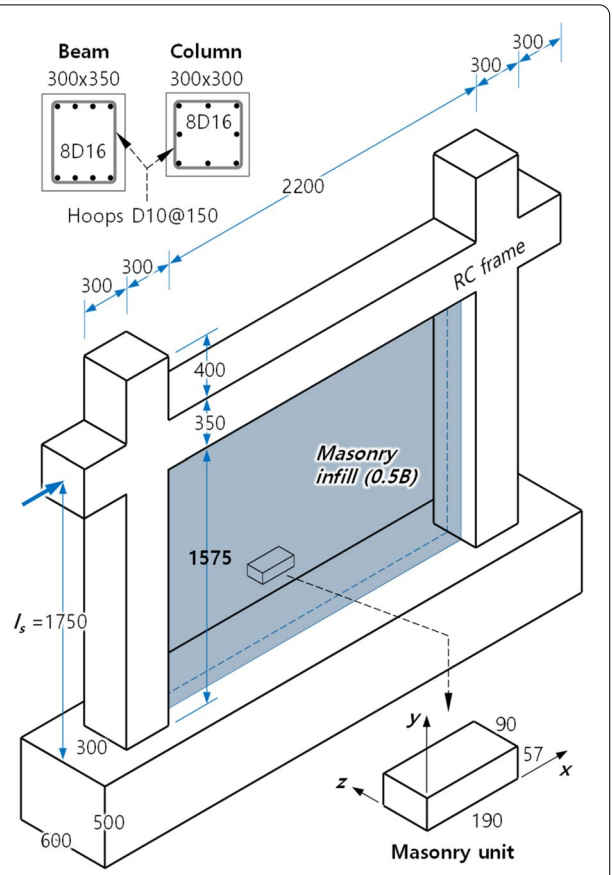

Fig. 4 Reinforced concrete moment frames with and without masonry infill tested by Kim et al. (2016).

bricks was 190 mm × 90 mm × 57 mm and the thickness of the bed and head mortar joints was 10 mm.

The material properties of the concrete, reinforcing steel bars, and masonry infill were as follows. For the concrete, the compressive strength was f_c' = 35.9 MPa. For the reinforcing steel bars, the yield strength (ultimate strength) of the D16 and D10 bars was f_y = 368 MPa and 440 MPa (f_u = 554 MPa and 597 MPa), respectively. For the masonry infill, the compressive strength and elastic modulus, obtained from the compression tests of 190 mm × 190 mm masonry prisms, were f_m' = 10.3 MPa and E_m = 2064 MPa, respectively. Such elastic modulus was significantly less than the design value E_m = 750 fm' = 7725 MPa specified in Uniform Building Code (IBC 1997), and consequently the strain at f_m' = 10.3 MPa was significantly increased to ε_{mo} = 0.0066 mm/mm. The cohesion and frictional coefficient on the mortar joint–cement brick interface were c = 0.602 MPa and μ = 1.18, respectively. Such c and μ were determined under monotonic loading and thus were greater than the design values of Eurocode 6 (ECS 2005), c = 0.1 MPa ~ 0.4 MPa and μ = 0.75.

4.2 Modeling Implementation for Analysis

The finite element modeling of the infilled frame specimens was implemented by VecTor2 (Wong et al. 2013). For the reinforced concrete frame members including the base, the concrete continuum was mostly modeled as BDR (bilinear displacement rectangle) elements using auto-mesh function in VecTor2; for IF0.5, CST (constant strain triangle) elements were partially included in the beam. The reinforcing steel bars were separately modeled as truss elements. Such reinforcement elements were placed at the actual locations. The masonry infills used in IFS0.5 and IF0.5 were modeled as BDR elements, and the mesh size was less than the brick size (i.e., 190 mm × 57 mm). For IFS0.5, the gap 35 mm was modeled as the long and narrow opening on top of the masonry infill under the beam.

Material models of the concrete and steel reinforcement used for analysis in VecTor2 were as follows. For the concrete under compression (f_c' = 35.9 MPa at strain ε_{co} = 0.002 mm/mm), a parabolic–linear model was used; strength increase due to confinement was not considered. The compression softening in cracked concrete due to transverse tensile strains was considered using the Vecchio and Collins 1986a model. For the tensile behavior of the concrete, the tensile strength was taken as $f_{ct} = 0.21\sqrt{f_c'} = 1.26$ MPa; before cracking, the linear elastic behavior with $E_c = 4500\sqrt{f_c'} = 27{,}000$ MPa was used; the tension-softening behavior after cracking was also assumed as linear. Details of the concrete model are presented in Wong et al. (2013). For the longitudinal and horizontal reinforcements, the tri-linear model based on the actual yield and ultimate strengths was used to represent the yield plateau and subsequent hardening behavior; bond slip and buckling were not considered.

To represent the orthotropic behavior of the masonry infill, the compressive strengths (f_{mx} and f_{my}), tensile strengths (f_{mtx} and f_{mty}), and elastic moduli (E_{mx} and E_{my}) in the x and y directions were defined as follows. For the y direction that is perpendicular to the bed joint, f_{my} and E_{my} were taken as the compressive strength f_m' = 10.3 MPa and elastic modulus E_m = 2064 MPa, respectively, obtained from the compression testing of masonry prisms. For the x direction, f_{mx} and E_{mx} were taken as 0.5 fm' and 0.5E_m, respectively, which are default input values in VecTor2 (Wong et al. 2013). In general, masonry walls are weak to horizontal cracking because the bed joints are continuous and straight. Such horizontal cracking may cause compression softening along the x direction; thus, f_{mx} and E_{mx} were reduced by 50% (ASCE 2000). For the compressive stress–strain relationships, the Hoshikuma et al. (1997) model embedded in VecTor2 (Wong et al. 2013) was used; in this model, the strain at the peak compressive stress was taken as

the value obtained from the test, $\varepsilon_{mo}=0.0066$ mm/mm. For the tensile strength of the masonry infill, the diagonal tension strength f_{dt} ($=0.125\sqrt{f_m'}$) specified in FEMA 356 (ASCE 2000) was used: $f_{mtx}=f_{mty}=0.125\sqrt{10.3}=0.401$ MPa. Note that masonry walls generally exhibit orthotropic behavior and thus the tensile strengths in the x and y directions may be different, as with the compressive strengths; however, actual masonry tensile strength was not reported in Kim et al. (2016), and thus in this study, the tensile strength of the masonry infill in the x and y directions were considered as same, due to lack of information.

The cohesion c and friction coefficient μ on the mortar joint–cement brick interface were determined based on the design values specified in Eurocode 6 (ECS 2005), as follows: the cohesion was taken as $c=0.1$ MPa (lower bound) and 0.4 MPa (upper bound); and the friction coefficient and angle on the interface were assumed as $\mu=0.75$ and $\phi=37°$. Note that, when masonry infill is subjected to cyclic loading, the shear resistance on the mortar joint–brick interface may be deteriorated as damage such as cracking and slip is accumulated during repeated load reversals. Thus, the c and μ values used for the analysis were adjusted to be less than the values obtained from the monotonic loading test (i.e., $c=0.602$ MPa and $\mu=1.18$).

4.3 Comparison of Analysis and Test Results

Figure 5 shows the lateral load–drift ratio (P–δ) relationships of BF, IF0.5, and IFS0.5. The tests were conducted under cyclic loading, while the analysis was performed under monotonic loading. Thus the P–δ curves by the test and analysis were compared only for positive loading. The analysis was performed for two cohesion strengths, $c=0.1$ and 0.4 MPa, and both results are plotted in Fig. 5. Note that the P–δ behavior of the infilled frames was different depending on loading directions; since the damage at the interface (such as cracking and interface sliding) that occurred in positive loading had impacts on the behavior under subsequent negative loading, the infilled frames displayed slightly smaller stiffness and strength under negative loading, than those under positive loading. Figure 5 also compares the failure modes of IF0.5 and IFS0.5 by the analysis and test. The photos of IF0.5 and IFS0.5 were taken after and during the test, respectively. The deformation mode and crack distribution obtained from the analysis were the results at the failure points (i.e., $\delta=4.7\%$ for IF0.5 and 4.2% for IFS0.5).

Overall, the P–δ curves by the analysis agreed well with the test results not only in the bare frame BF, but in the infilled frames, IF0.5 and IFS0.5. In particular for $c=0.4$ MPa (see Fig. 5b and c), the predicted pre-peak behavior was in good agreement with the test curves. On the other hand, the post-peak behavior, such as strength degradation and ductility, slightly differed from the tests; the analysis estimated steeper strength degradation and less ductile behavior, compared to the test results. Note that when compared to IF0.5 where the masonry infill was compactly installed within the frame, the initial stiffness and peak strength of IFS0.5 with gap (i.e., poor mortar filling) along the horizontal boundary of the masonry infill under the beam were significantly degraded. The VecTor2 analysis accurately estimated the difference in the pre-peak behavior between IF0.5 and IFS0.5.

Figure 5b and c shows the deformation mode and crack distributions of the masonry infills, predicted by the analysis. Although the deformation modes under lateral loading were almost same, the crack distribution of IFS0.5 completely differed from that of IF0.5 due to poor mortar filling along the boundary under the beam. For IF0.5, the cracks were distributed over the entire area of the masonry infill. However, for IFS0.5, the cracks mainly occurred in a triangle area enclosed by the tension column (vertical) and bottom base (horizontal); the inclination of diagonal cracks in the masonry infill (or diagonal struts) was relatively small; and vertical cracks were obvious along the boundary between the compression column and masonry infill. Such crack distributions agreed well with the failure aspects observed from the tests.

4.3.1 Diagonal Strut Actions of Masonry Infill

In this study, through nonlinear analysis using VecTor2, the behavior of masonry-infilled frames, such as the early cracking on the masonry infill and consequent force transfer to the adjacent columns, was investigated. In particular, this study focused on failure mode and force transfer mechanism depending on: (1) relative stiffness and strength between the masonry infill and adjacent columns and (2) poor mortar filling on the masonry boundary under the beam (i.e., substandard masonry-infilled frame). For this purpose, nonlinear analysis was performed for four infilled frame specimens, IF0.5, IFS0.5, IF1.0, and IFS1.0 tested by Kim et al. (2016). IF1.0 and IFS1.0 were the specimens in which the thickness of masonry infill was increased to 1.0B or 190 mm.

Noe that the cohesion on the mortar joint–brick interface significantly affects analysis result. For IF0.5 and IFS0.5 in Fig. 5b and c, as the cohesion c increased from 0.1 MPa to 0.4 MPa, the initial stiffness, peak strength, and post-peak strength increase. However, it is impossible to accurately determine the cohesion and frictional coefficient because they continuously vary with damage

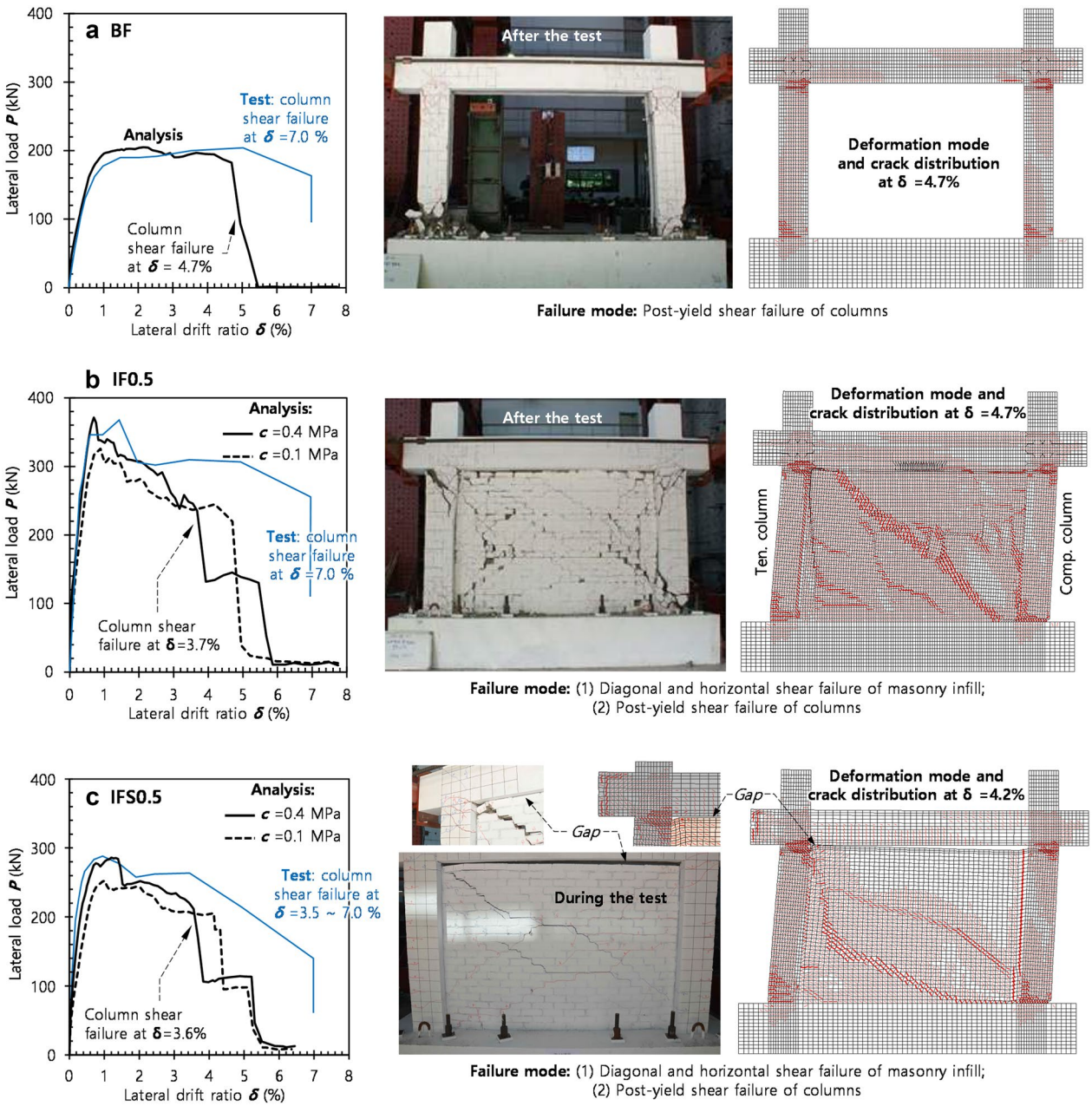

Fig. 5 Lateral load–drift ratio relationship and failure mode: test vs. analysis.

on the interface even while conducting test. Thus, in the following subsections, the cohesion strengths that yielded best agreements with the test results were used for nonlinear analysis: $c = 0.4$ MPa for IF0.5 and IFS0.5 and $c = 0.602$ MPa for IF1.0 and IFS1.0.

4.4 Standard Masonry-Infilled Frames: IF0.5 and IF1.0

Figure 6 shows the distributions of minimum principal compressive stresses (i.e., f_{m2} for masonry element and f_{c2} for concrete element) at the elastic limit, peak, and residual points for IF0.5. The elastic limit point (E) indicates the pre-peak point at which the strength reached 70% of the peak strength and thus the masonry infill began to separate from the frame members (ASCE/SEI 2017); the peak point (P) is defined as the point at which the strength was greatest; and the residual point (R1 and R2) indicates the post-peak points that were reached after the significant strength degradation. The distributions of

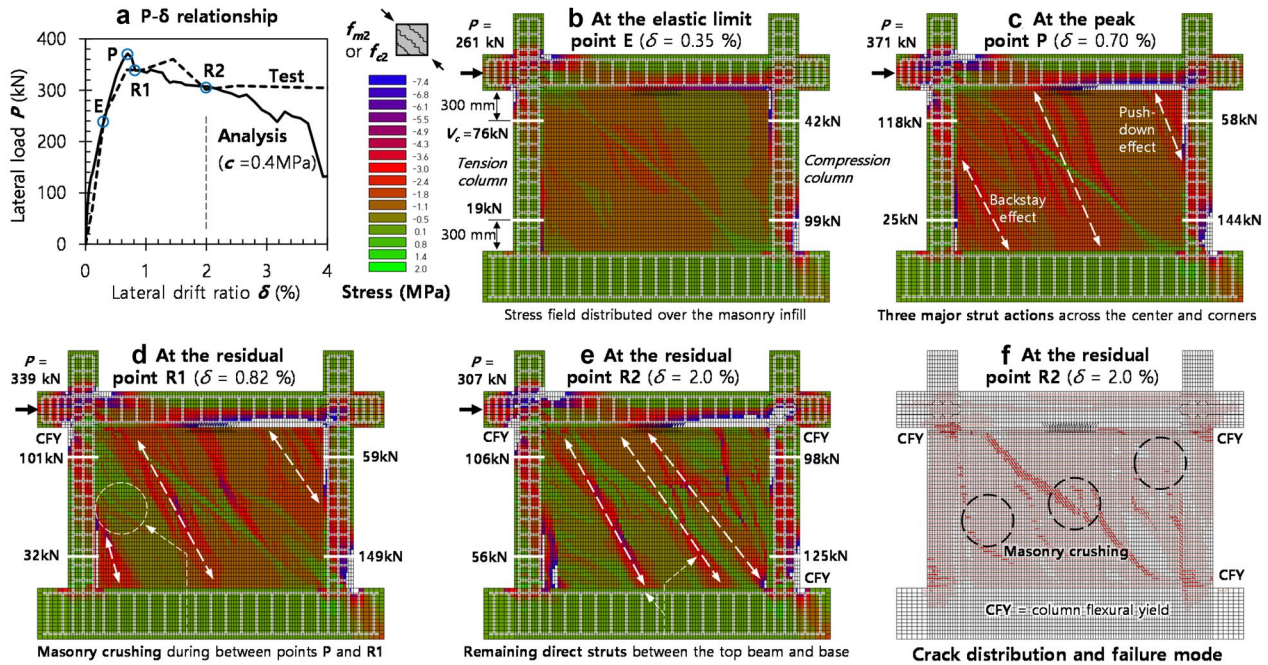

Fig. 6 Variation of stress distribution and force transfer with deformation: standard infilled frame IF0.5–weak masonry infill.

diagonal compressive stresses, f_{m2} in the masonry infill and f_{c2} in the concrete frame, are presented as color contour; green color indicates tensile stresses, whereas red and blue colors indicate compressive stresses. The crack distribution at the residual point R2 is also presented in Fig. 6f. The analysis results of IF1.0 where the thickness

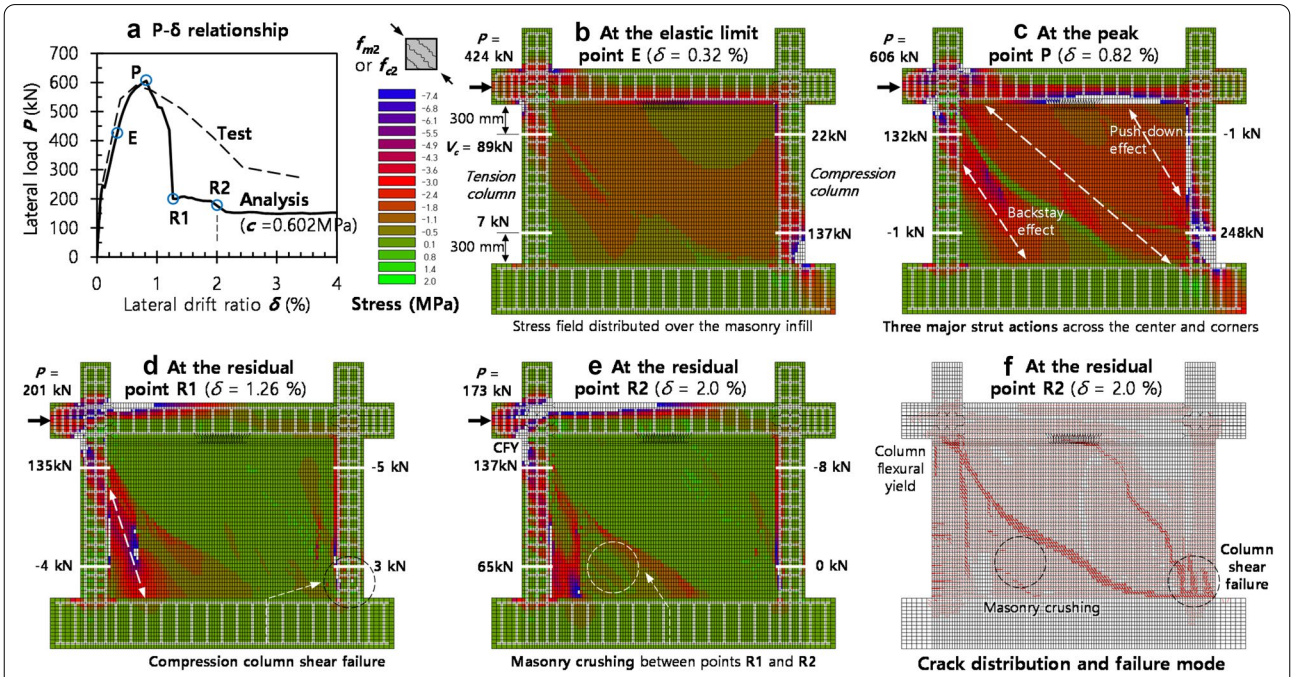

Fig. 7 Variation of stress distribution and force transfer with deformation: standard infilled frame IF1.0–strong masonry infill.

of the masonry infill was increased to 1.0B or 190 mm are shown in Fig. 7. For easier distinction between IF0.5 and IF1.0 with different masonry thickness, Figs. 6 and 7 are referred as the analysis results for 'weak masonry infill' and 'strong masonry infill', respectively. Since lateral loading is applied from the left to the right, the left and right columns are denoted as tension and compression columns, respectively. For these columns, shear forces acting on the section located at a distance 300 mm (=column depth) from the bottom base and top beam ($=V_c$) are presented in Figs. 6 and 7.

The behavioral characteristics of the standard infilled frames IF0.5 and IF1.0 can be summarized as follows:

(1) *Elastic limit point (E)*

The elastic limit points corresponding to 70% of the peak strength, were reached at $\delta=0.35\%$ and 0.32% for IF0.5 and IF1.0, respectively (see Figs. 6b and 7b)). In both specimens, diagonal cracks already occurred on the masonry infill, and the diagonal compressive stresses (f_{m2}) were almost uniformly distributed. The compression columns were subjected to greater shear force at these elastic limit points.

(2) *Peak point (P)*

The peak points were reached at $\delta=0.7\%$ and 0.82% for IF0.5 and IF1.0, respectively (see Figs. 6c and 7c). At the peak points, the distribution of diagonal compressive stresses was non-uniform in both specimens. The strut actions on the masonry infill mainly occurred along three load paths, two of which were the strut actions forming around the corners of the tension and compression columns; the remaining one was the direct strut action between the top beam and bottom base across the masonry infill. In this study, the strut action forming at the bottom corner of the tension column was defined as the 'backstay action', whereas the strut action forming at the top corner of the compression column was defined as the 'push-down action'. The effects of such backstay and push-down actions on the frame behavior were discussed in detail in the next section "Effects of backstay and push-down actions on column shear failure".

(3) *Residual points (R1 and R2)*

The first residual points R1 indicate the points where the strength was significantly decreased immediately after the peak strength (i.e., $\delta=0.82\%$ and 1.26% for IF0.5 and IF1.0, respectively, see Figs. 6a and 7a). In this strength degradation stage, IF0.5 and IF1.0, classified as 'weak masonry infill' and 'strong masonry infill', respectively, displayed completely different failure aspects, as follows.

For IF0.5 (see Fig. 6a and d), the lateral strength decreased as crushing failure occurred in the thin masonry infill near the tension column. As the deformation gradually increased to the second residual point R2 ($\delta=2.0\%$), such masonry crushing prevailed over the whole area of the masonry infill. Consequently, the strut actions around the corners, associated with the backstay and push-down actions, almost vanished, as shown in Fig. 6e. The tension and compression columns underwent flexural yielding during the post-peak behavior between points R1 and R2, except at the bottom of the tension column. Figure 6f shows that the failure mode of IF0.5 with 'weak masonry infill' was crushing of the thin masonry infill and subsequent flexural yielding of columns.

For IF1.0 (see Fig. 7a and d), at the first residual point R1, the lateral strength significantly decreased from 606 to 201 kN as brittle shear failure occurred at the bottom of the compression column where the strut actions were concentrated. Due to such column shear failure, the strut actions on the masonry infill almost vanished, except near the tension column (i.e., backstay action); instead, the thick masonry infill did not undergo crushing failure. As the deformation gradually increased to the second residual point R2 ($\delta=2.0\%$), the strength was maintained as nearly constant. Figure 7e shows that the tension column and backstay strut action contributed to the residual strength. In this stage, the tension column underwent flexural yielding at the top. Figure 7f shows that the failure mode of IF1.0 with 'strong masonry infill' was shear failure of the compression column (bottom) and subsequent flexural yielding of the tension column.

5 Substandard Masonry-Infilled Frames: IFS0.5 and IFS1.0

Figures 8 and 9 show the analysis results of substandard infilled frames, IFS0.5 and IFS1.0 with poor mortar grouting on the boundary between the masonry infill and top beam (i.e., gap 35 mm). IFS0.5 and IFS1.0 with different masonry thickness, 0.5B and 1.0B, respectively, can be regarded as 'weak masonry infill' and 'strong masonry infill'. The behavioral characteristics of the substandard infilled frames can be summarized as follows:

(1) Elastic limit point (E)

The elastic limit points corresponding to 70% of the peak strength, were reached at $\delta=0.32\%$ and 0.28% for IFS0.5 and IFS1.0, respectively (see Figs. 8b and 9b). During such early loading stage, both specimens underwent large vertical cracks along the boundary of the compression column. This indi-

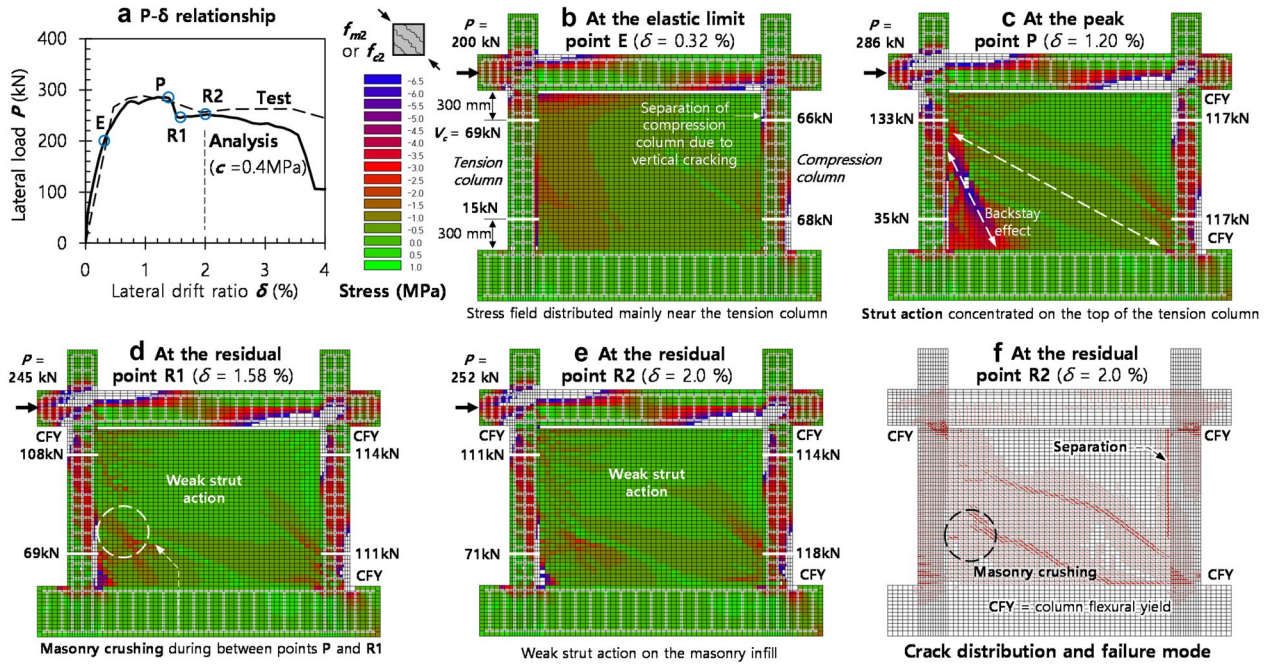

Fig. 8 Variation of stress distribution and force transfer with deformation: substandard infilled frame IFS0.5–weak masonry infill.

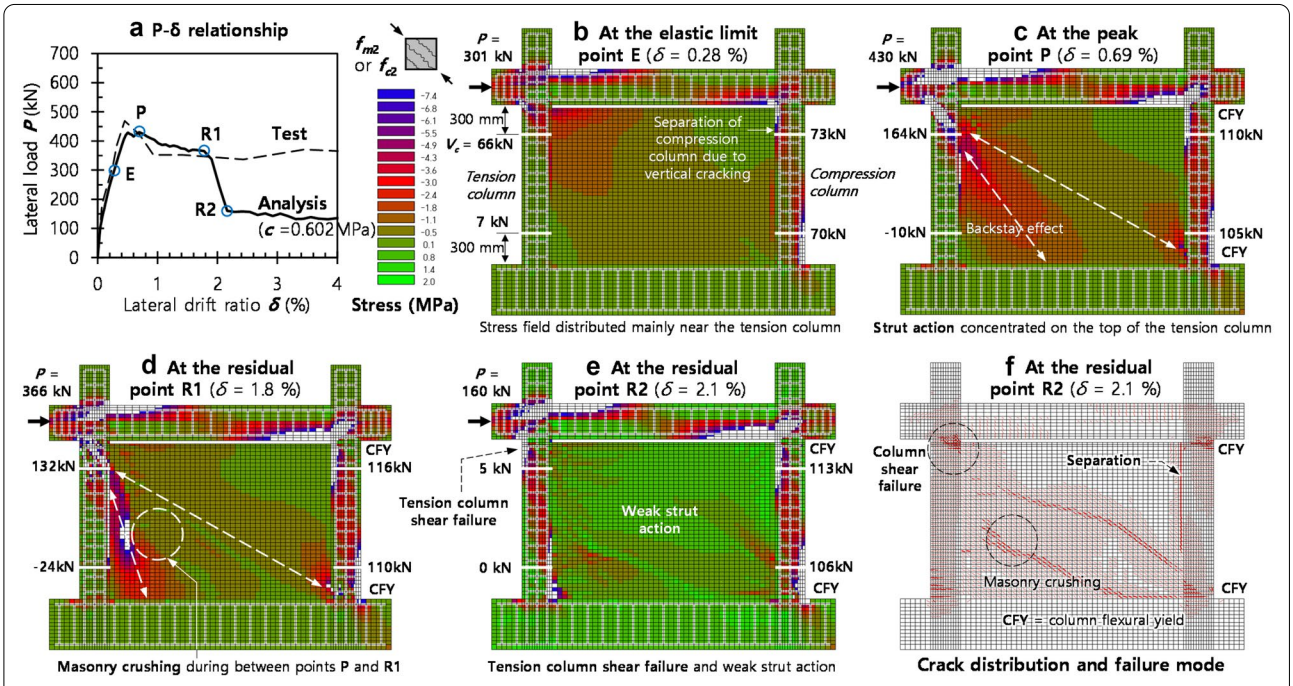

Fig. 9 Variation of stress distribution and force transfer with deformation: substandard infilled frame IFS1.0–strong masonry infill.

cates that the compression column behaved as an independent column. Overall, diagonal compressive stresses of the masonry infill were mainly distributed near the tension column.

(2) Peak point (P)

The peak points were reached at $\delta = 1.2\%$ and 0.69% for IF0.5 and IF1.0, respectively (see Figs. 8c and 9c). At the peak points, the strut actions on the masonry infill mainly occurred along two load paths; one was the 'strong' backstay action forming near the tension column and the other was the 'weak' strut action forming along the diagonal line between the top of the tension column and the bottom of the compression column.

(3) Residual points (R1 and R2)

The behavior at the residual points R1 and R2 were different in IFS0.5 and IFS1.0, as follows.

For IFS0.5 with 0.5B masonry thickness (see Fig. 8a and d), the lateral strength decreased at point R1 as crushing failure occurred in the thin masonry infill near the tension column. After that, strut actions on the masonry infill almost vanished; instead, the tension and compression columns underwent flexural yielding, except at the bottom of the tension column. Consequently, IFS0.5 displayed post-peak ductile behavior during points R1 and R2. Figure 8f shows that the failure mode of IFS0.5 with 'weak masonry infill' was flexural yielding of the columns and subsequent crushing of the thin masonry wall.

For IFS1.0 with 1.0B masonry thickness (see Fig. 9a and d), the lateral strength was gradually degraded from 430 to 360 kN during points P and R1, as masonry crushing failure occurred locally near the tension column. At point R2, the tension column underwent brittle shear failure at the top, and thus strut actions on the masonry infill almost vanished. Consequently, the lateral strength significantly decreased from 366 kN at point R1 to 160 kN at point R2. The residual strength after point R2 was mainly contributed by the flexural strength of the compression column that underwent flexural yielding (see Fig. 9e). Figure 9f shows that the failure mode of IFS1.0 with 'strong masonry infill' was flexural yielding of the compression column and subsequent shear failure of the tension column (top).

6 Effects of Backstay and Push-Down Actions on Column Shear Failure

As shown in Figs. 6, 7, 8 and 9, the interaction between the masonry infill and columns in infilled frames can be defined as the backstay action near the tension column and the push-down action near the compression column. The backstay and push-down actions increase column forces such as axial and shear forces, and ultimately affect the strength, ductility, and failure mode of the infilled frames, as follows.

Figure 10 shows the column shear forces at the peak points P of IF0.5, IF1.0, IFS0.5, and IFS1.0. The column shear forces were obtained at the five points along the column length, and their variations were represented as piecewise linear profiles connecting the values at the five

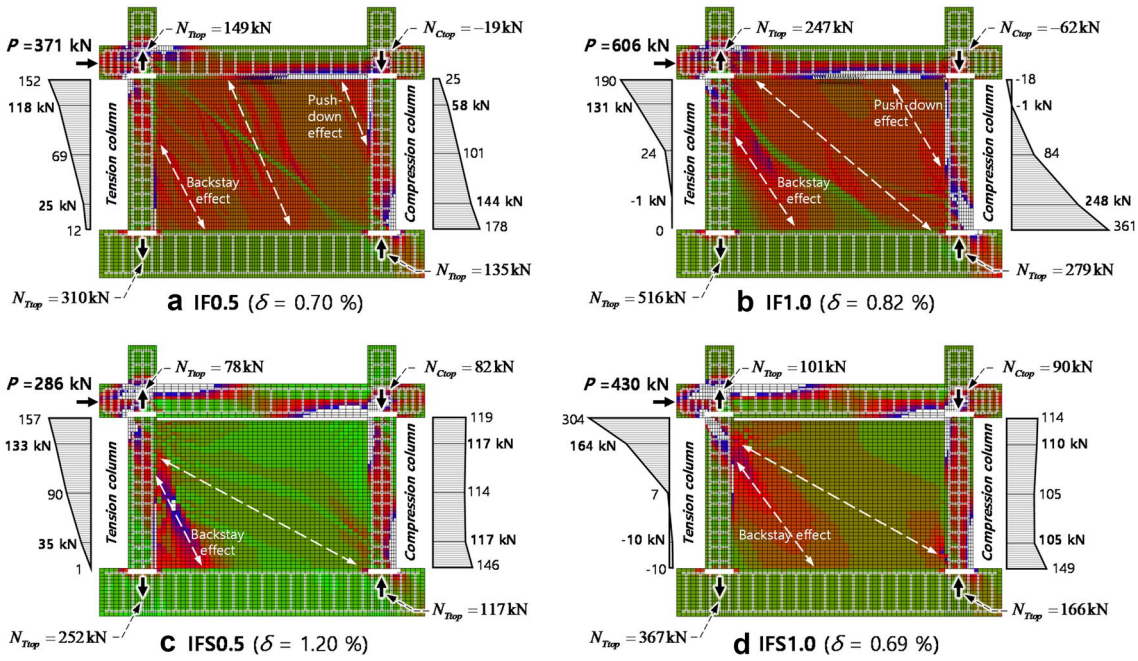

Fig. 10 Distributions of column shear and axial forces at the peak point.

points. For the tension columns on the left side, shear forces decreased almost linearly from the maximum value at the top to zero at the bottom, as a portion of the shear force went out by means of the masonry struts at the bottom (i.e., backstay effects). The decreasing rate of shear forces was greater in IF1.0 and IFS1.0 with thicker masonry infill (i.e., 1.0B). However, the shear force distributions in the compression columns on the right side differed depending on the presence of poor mortar grouting on the masonry boundary under the beam. For standard infilled frames IF0.5 and IF1.0 without poor mortar grouting (see Fig. 10a and b), shear forces increased almost linearly from zero at the top to the maximum value at the bottom, as the masonry diagonal struts located near the top corner of the frame transferred lateral forces to the column (i.e., push-down effects). For the substandard infilled frames IFS0.5 and IFS1.0 with poor mortar grouting (see Fig. 10c and d), diagonal strut action did not form near the top corner of the frame on the right side, and thus the compression columns independently behaved without push-down effects. Consequently, the compression columns were subjected to almost uniform shear along the height.

As shown in Figs. 7 and 9, IF1.0 and IFS1.0 exhibited column shear failure during the post-peak behavior. For IF1.0, column shear failure occurred at the bottom of the compression column and the shear force near the critical section (i.e., 300 mm high from the base) was $V_u = 248$ kN (see Figs. 7c or 10b). In contrast, for IFS1.0, column shear failure occurred at the top of the tension column, and the shear force near the critical section (i.e., 300 mm below the beam) was $V_u = 164$ kN (see Figs. 9c or 10d). The difference in column shear forces at the point of shear failure might be explained by the variation in column axial forces depending on the backstay and push-down effects, as follows:

- For the compression column in IF1.0, the axial compression force was increased to $N_{Cbot} = 279$ kN at the bottom, due to the push-down action (see Fig. 10b). Thus, column shear failure occurred at $V_u = 248$ kN, which was greater than the nominal shear strength $V_n = 191$ kN $(= V_c + V_s = \sqrt{f_c'}bd/6 + f_{yv}A_v d/s)$ (ACI 318–14).
- For the tension column in IFS1.0, the axial tension force was $N_{Ttop} = 101$ kN at the top (see Fig. 10d). Since the tension force decreased the shear strength contributed by concrete (i.e., V_c), column shear failure occurred at $V_u = 164$ kN that was less than the nominal shear strength $V_n = 191$ kN.

The axial forces in the columns continuously vary along their height. The variation of axial forces in the columns can be explained by the shear transfer at the interface between the masonry infill and columns, as follows. Figure 11 shows the distributions of shear stresses v_m that

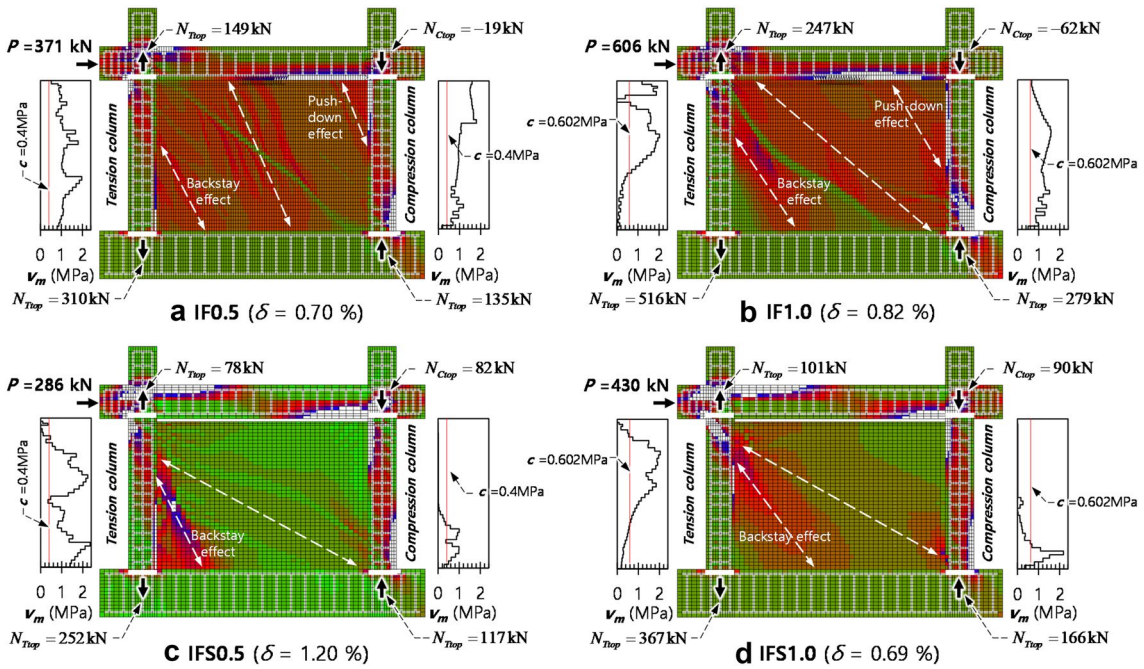

Fig. 11 Distributions of interface shear stresses on the boundary of masonry infill and concrete column.

occurred along the boundary between the masonry infill and concrete column. The direction of v_m was upward on the boundary of the tension column and downward at the boundary of the compression column. The distributions of v_m were obtained at the peak points (P) from the analysis. The shear strength v_m of the mortar joint–column interface, determined from Eq. (7), was large at the boundary where the backstay and push-down strut actions of the masonry infill were concentrated. In all specimens, the maximum values of v_m were greater than the cohesion strength (i.e., $c = 0.4$ MPa for IF0.5 and IFS0.5 and $c = 0.602$ MPa for IF1.0 and IFS1.0), due to the presence of normal compressive stresses on the masonry wall–concrete column interface (see σ_{nj} in Fig. 3b). Here, the differential axial forces between the top and bottom of the tension and compression columns, $(N_{Tbot} - N_{Ttop})$ and $(N_{Cbot} - N_{Ctop})$, respectively, can be the determined by integrating v_m along the vertical interface:

$$\left(N_{Tbot} - N_{Ttop}\right) \text{ or } \left(N_{Cbot} - N_{Ctop}\right) = \int_{h_m} v_m t_m dy, \tag{8}$$

where h_m and t_m are the height and thickness of the masonry infill. Equation (8) clearly shows that the backstay and push-down actions increase the axial tension and compression forces at the bottom of the columns, respectively.

Note that, shear failure of the tension column occurred not at the bottom where the axial tension force was the greatest, but at the top where the axial tension force was significantly reduced (i.e., Equation (8)). This indicates that although the backstay action significantly increases the axial tension force at the bottom of the right column, such increased tension force may not significantly affect the column shear resistance.

7 Conclusions

This study investigated the behavior of masonry-infilled reinforced concrete frames through nonlinear finite element analysis. By comparing the distributions of cracks and diagonal struts on the masonry infill at various loading stages, the effects of such diagonal strut actions on the masonry infill-frame interaction and column shear failure were studied. The major findings are as follows:

(1) Nonlinear finite element analysis by VecTor2 estimated with reasonable precision the lateral load–deformation response and failure mode of the infilled frames affected by design variables, such as the thickness of the masonry infill and poor mortar filling on the masonry boundary under the beam. This indicates that the DSFM and hyperbolic Mohr–Coulomb yield criterion for masonry, adopted in VecTor2, were appropriate to accurately simulate the complex behavior on the mortar joint–brick interface.

(2) For infilled frames where the masonry wall is compactly filled without gap, the strut actions on the masonry infill mainly occurred along three load paths: (a) backstay strut action near the bottom of the tension column, (b) push-down strut action near the top of the compression column, and (c) direct strut action between the top beam and bottom base across the masonry infill. On the other hand, for infilled frames where there was a gap on the masonry boundary under the beam, only two strut actions (i.e., the backstay strut action and direct strut action) occurred, as the compression column behaved independently.

(3) Brittle shear failure occurred in the columns of the infilled frame specimens with thick masonry thickness 1.0B, as the backstay or push-down strut actions increased column shear force. Such column shear failure differed depending on the presence of poor mortar filling: the infilled frame without poor mortar filling exhibited shear failure at the bottom of the compression column, whereas the infilled frame with poor mortar filling exhibited shear failure at the top of the tension column. For the infilled frame specimens with thin masonry thickness 0.5B, masonry crushing failure occurred before shear failure of columns, and thus the behavior was more ductile.

Although the finite element analysis was performed for monotonic loading, the results of the analysis were compared with those of cyclic loading tests. The comparison showed that the predicted behavior of the masonry-infilled frames, such as lateral load–deformation relationships and failure modes, agreed well with the behavior observed from the tests. Thus, the findings on the behavior of masonry-infilled frames may be applicable not only for monotonic loading, but also for cyclic loading.

The analysis results showed that the diagonal strut actions on the cracked masonry infill and consequent failure mode may be various depending on design variables, such as the masonry thickness, cohesion on the mortar joint–brick interface, and the presence of poor mortar filling. Thus, further study to improve the existing strut models for masonry-infilled frames is required.

Acknowledgements

This work was supported by the National Research Foundation of Korea (Grant Nos. NRF-R-2019-01064 and NRF-2018R1A6A1A07025819) and by the Ministry of the Interior and Safety of Korea (Grant No. 2020-MOIS32-029). The authors are grateful to their supports.

Authors' information
Mr. Seung-Jae Lee is a graduate student at the Department of Architecture of Dankook University in Korea. His research interests include the experiment and analysis of reinforced and masonry members. He has been also studying performance-based seismic evaluation and design of reinforced concrete building structures.

Prof. Tea-Sung Eom is an Associate Professor at the Department of Architecture of Dankook University in Korea. He received his BS, MS and Ph.D. Degrees from Seoul National University in Korea. His research interests include experiment and nonlinear analysis of reinforced concrete, steel and composite structures. He is also studying seismic evaluation and retrofit of existing building structures.

Prof. Eunjong Yu is an Associate Professor at the Department of Architectural Engineering at Hanyang University in Korea. His research interests include experiment and nonlinear analysis of reinforced concrete and masonry structures. He is also studying seismic evaluation and retrofit of existing building structures.

Authors' contributions
S-JL performed nonlinear finite element analysis of masonry-infilled reinforced concrete frames. T-SE contributed to writing the manuscript as the principle author. He analytically investigated the behavior of masonry-infilled reinforced concrete frames subjected to lateral load. EY provided test data included in the manuscript. In addition, he contributed to writing and reviewing the manuscript. His suggestions and comments improved the completeness and readability of the manuscript. All authors read and approved the final manuscript.

Funding
This work was supported by the National Research Foundation of Korea (Grant Nos. NRF-2019R1F1A1059248 and NRF-2018R1A6A1A070258) and by the Ministry of the Interior and Safety of Korea (Grant No. 2020-MOIS32-029).

Availability of data and materials
Not applicable.

Competing interests
Not applicable.

Author details
[1] Dept. of Architectural Engineering, Dankook Univ., 152 Jukjeon-ro, Gyeonggi 16890, Korea. [2] Dept. of Architectural Engineering, Hanyang Univ., Wangsimni-ro, Seongdong-gu, Seoul 22204763, Korea.

Received: 2 January 2020 Accepted: 19 September 2020
Published online: 29 January 2021

References

ACI Committee 318. (2014). *Building Code Requirements for Structural Concrete, ACI 318–14*. Farmington Hills, MI: American Concrete Institute.
Applied Technology Council (ATC) (1998), *Evaluation of Earthquake Damaged Concrete and Masonry Wall Buildings – Basic Procedures Manual*, FEMA 306, Federal Emergency Management Agency, Washington D.C.
Al-Chaar, G. (2002), *Evaluating Strength and Stiffness of Unreinforced Masonry Infill Structures.* Report No. ERDC/CERL TR-02–1, US Army Corps of Engineers.
American Society of Civil Engineers (ASCE) / Structural Engineering Institute (SEI). (2017). *Seismic Rehabilitation of Existing Buildings, ASCE/SEI 41–17*. Reston, Virginia: American Society of Civil Engineers.
American Society of Civil Engineers (ASCE) (2000), *Prestandard and Commentary for the Seismic Rehabilitation of Buildings*, FEMA 356, Federal Emergency Management Agency, Washington D.C.
Angelillo, M., Lourenco, P. B., and Milani, G. (2014). "Masonry behaviour and modelling", *Mechanics of Masonry Structures* (Part of the International Centre for Mechanical Sciences book series, (CISM, 551).
Architectural Institute of Korea (AIK). (2016). *Korean Building Code – Structural (KBC 2016)*. Seoul, Korea: Architectural Institute of Korea.
Atkinson, R. H., Amadei, B. P., Saeb, S., & Sture, S. (1989). Response of masonry bed joints in direct shear. *Journal Structural Engineering, 115*(9), 2276–2296.
Crisafulli, F.J. (1997), *Seismic behaviour of reinforced concrete structures with masonry infills*, Ph.D. Dissertation, University of Canterbury, New Zealand.
Dolsek, M., & Fajfar, P. (2002). Mathematical modelling of an infilled RC frame structure based on the results of pseudo-dynamic tests. *Earthquake Engineering and Structural Dynamics, 31*(6), 1215–1230.
El-Dakhakhni, W. W., Mohamed, E., & Hamid, A. A. (2003). Three-strut model for concrete masonry-infilled steel frames. *Journal of Structural Engineering, 129*(2), 127–185.
European Committee for Standardization (ECS) (2005). *Eurocode 6: Design of masonry structures, Part 1.1: General rules for reinforced and unreinforced masonry structures.* Belgium, 2005.
Facconi, L., Fausto, M., & Vecchio, F. J. (2018). Predicting Uniaxial Cyclic Compressive Behavior of Brick Masonry: New Analytical Model. *Journal of Structural Engineering, 144,* 2.
Facconi, L., Plizzari, G., & Vecchio, F. J. (2014). Disturbed stress field model for unreinforced masonry. *Journal of Structural Engineering, 140,* 4.
Kim, C., Yu, E., & Kim, M. (2016). Finite element analysis of reinforced concrete masonry infilled frames with different masonry wall thickness subjected to in-plane loading. *Journal of the Computational Structural Engineering Institute of Korea, 29*(1), 85–93.
Lourenco, P. B., & Rots, J. G. (1997). Multisurface interface model for analysis of masonry structures. *Journal of Structural Engineering, 123*(7), 660–668.
Lourenco, P. B., Rots, J. G., & Blaauwendraad, J. (1998). Continuum model for masonry: Parameter estimation and validation. *Journal of Structural Engineering, 124*(6), 642–652.
Mehrabi, A. B., & Shing, P. B. (1997). Finite element modeling of masonry-infilled RC frames. *Journal of Structural Engineering, 123*(5), 604–613.
Park, J. H., Jeon, S. H., & Kang, K. S. (2012). Seismic performance evaluation of masonry-infilled frame structures using equivalent strut models. *Journal of the Earthquake Engineering Society of Korea, 16*(1), 47–59.
Paulay, T., & Priestley, M. J. N. (1992). *Seismic Design of Reinforced Concrete and Masonry Buildings*. USA: Wiley.
Rahman, A., & Ueda, T. (2014). Experimental investigation and numerical modeling of peak shear stress of brick masonry mortar joint under compression. *Journal of Materials in Civil Engineering, 26,* 9.
Rots, J. G. (1997). *Structural Masonry: An Experimental/Numerical Basis for Practical Design Rules*. Rotterdam, The Netherlands: Balkema.
Stafford-Smith, B. (1966). Behavior of square infilled frames. *Journal of the Structural Division, ASCE, 92*(1), 381–404.
Stavridis, A., & Shing, P. B. (2010). Finite-element modeling of nonlinear behavior of masonry-infilled RC frames. *Journal of Structural Engineering, 136*(3), 285–296.
Wong, P. S., Vecchio, F. J., & Trommels, H. (2013). *VecTor2 & FormWorks User's Manual (Second Edition)* (p. 318). Department of Civil Engineering: University of Toronto, Toronto.
Yu, E. J., Kim, M. J., & Jung, D. G. (2016). A comparative study of equivalent strut models for seismic performance evaluation of masonry-infilled frame. *Journal of the Earthquake Engineering Society of Korea, 18*(2), 79–87.
Zhai, C., Wang, X., Kong, J., Li, S., & Xie, L. (2017). Numerical simulation of masonry-infilled RC frames using XFEM. *Journal of Structural Engineering, 143,* 10.

Publisher's Note